



Fine-tuning copper dispersion in Cu/SiO₂ core-shell particles regulates electrochemical CO₂ reduction product selectivity

Tianying Zhang^{a,1}, Yaxin Jin^{a,1}, Shi Nee Lou^{a,b,*}, Tianxiang Yan^a, Tiantian Xiao^a, Zhihui Liu^a, Jianlong Lin^a, Siyu Kuang^a, Sheng Zhang^{a,b,*}, Xinbin Ma^{a,b}

^a Key Laboratory for Green Chemical Technology of Ministry of Education, Collaborative Innovation Centre of Chemical Science and Engineering, School of Chemical Engineering and Technology, Tianjin University, Tianjin 300072, China

^b Haihe Laboratory of Sustainable Chemical Transformations, Tianjin 300072, China

ARTICLE INFO

Keywords:

Cu/SiO₂ core-shell particles
Electrochemical CO₂ reduction
Dispersion modulation
Product selectivity

ABSTRACT

The wide product spectrum resulting from the intricate reactions of electrochemical CO₂ reduction reaction (CO₂RR) makes CO₂RR unfavorable for industrial electrolysis. Herein, we demonstrate a hydrogen-feeding effect from copper-silica catalysts that can regulate CO₂RR product selectivity via modulation of Cu dispersion in the copper-silica core-shell particles. We found electromethanation of CO₂ is greatly enhanced on Cu-Si catalyst with optimally dispersed Cu nanoparticles, resulting in a high methane Faradaic efficiency of 72.9 %. In contrast, a lower or higher Cu dispersion correlated to a preferential (co-)production of methane and ethylene or hydrogen. Combining density functional theory (DFT) calculations and spectroscopic analysis, we show Cu dispersion affects the Cu coverage on SiO₂ and the exposure of Cu-O-Si interfacial sites for CO₂RR and water dissociation. An optimum Cu dispersion creates abundant Cu-O-Si sites with reduced energy barriers for both the hydrogenation of *CHO and water dissociation, leading to selective methane formation.

1. Introduction

CO₂RR, powered by renewable electricity, offers a promising approach for closing carbon footprints and CO₂ utilization [1,2]. As an alternative green technology to traditional energy-intensive industry, it features a promising route for CO₂ conversion to high value-added chemical feedstock [1]. Nevertheless, it faces the challenges of broad product spectrum, including CO and various C₁ and C₂₊ oxygenates and hydrocarbon products. Though the production of carbon monoxide or formate could be achieved with high selectivity (Faradaic efficiency >90 %) and high current density (>200 mA cm⁻²) concurrently [3–5], other products with a production process demanding more than two electrons are consistently hindered by inferior product selectivity with a product spectrum highly dependent on the characteristics of the copper-based catalysts [6,7].

While Cu-based electrodes such as oxides of Cu and their derivatives are widely reported to influence CO₂RR [8–10], the construction of effective Cu-support interfaces also present an opportunity to tune the

adsorption energies of CO₂RR intermediates thus affecting product selectivity [11]. For instance silicate-based materials, such as silica (SiO₂) and copper phyllosilicate (CuSiO₃), have in recent years emerged as effective supports for tuning CO₂RR product selectivity [6–12]. SiO₂ surface possesses abundant silanol groups with important effects on CO₂RR [12]. In addition, SiO₂ shows strong affinities with Cu and forms Cu-O-Si interface spontaneously [13–19]. Xiong et al. shows with the assistance of Si-O-H and Cu-Si-O interfaces, the *H and *CHO intermediates were effectively stabilized over a core-shell structured silica-copper catalyst (p-Cu@m-SiO₂), which could not only inhibit hydrogen evolution reaction but also promote *CHO-*CO coupling to form ethylene [12]. In particular, the formation of CuSiO_x or CuSiO₃ can enhance the metal-support interactions resulting in improved strength of Cu-O-Si interface [20]. CuSiO_x were shown to protect Cu⁺ species against reduction by forming Cu-O-Si bonds [14,15]. Moreover, the synergistic effect of Cu⁰-Cu⁺ pairs enhanced *CO adsorption and facilitated C-C coupling to lead to high C₂₊ products Faradaic efficiencies [14,16–18]. Recently, SiO₂ were also demonstrated to form SiO-H^{δ+} or

* Corresponding authors at: Key Laboratory for Green Chemical Technology of Ministry of Education, Collaborative Innovation Centre of Chemical Science and Engineering, School of Chemical Engineering and Technology, Tianjin University, Tianjin 300072, China.

E-mail addresses: snlou@tju.edu.cn (S.N. Lou), sheng.zhang@tju.edu.cn (S. Zhang).

¹ Tianying Zhang and Yaxin Jin contribute this article equally.

<https://doi.org/10.1016/j.apcatb.2024.124065>

Received 22 January 2024; Received in revised form 14 March 2024; Accepted 9 April 2024

Available online 10 April 2024

0926-3373/© 2024 Elsevier B.V. All rights reserved.

Si-H, which promote the hydrogenation of C=O bonds [19,21]. Considering the hydrogenation of *CO to form *CHO intermediate (*CO + *H → *CHO) is a critical step in CO₂RR, adequate proton feeding from water dissociation is also paramount for boosting CO₂RR performances. However, studies on the hydrogen-feeding effects of copper-silica catalysts from water dissociation and their impacts on CO₂RR performances are yet to be reported.

Herein, we report, for the first time, a promoted hydrogen-feeding effect from water dissociation over Cu-Si core-shell particle catalysts and, a rational copper dispersion-modulation strategy that can regulate Cu-O-Si exposed sites and tune C₁ and C₂ product selectivity from CO₂RR. Using a modified Stöber method, Cu_xSi core-shell particle catalysts with varied copper nanoparticle dispersion were prepared. Through comprehensive characterizations corroborated with DFT calculations, we correlated the product selectivity with dispersion of Cu moieties, furnishing fresh insights into the Cu-O-Si interface and the promoted *CO hydrogenation or C-C coupling over Cu-Si core-shell particle catalysts.

2. Experimental section

2.1. Materials

Cupric nitrate (Cu(NO₃)₂·3 H₂O, 99%) was purchased from Tianjin Damao. Polyvinylpyrrolidone (PVP, average molecular weight 8000, K16–18), tetraethyl orthosilicate (TEOS, >99%), ammonium chloride (NH₄Cl, ≥99.5%) and potassium bicarbonate (KHCO₃, 99.9%) were purchased from Shanghai Macklin Biochemical Co., Ltd. Cetyl trimethyl ammonium bromide (CTAB, 99%) was obtained from Tianjin GuangFu Technology Development Co., Ltd. Ammonia solution (25–28%) was obtained from Shanghai Yien Chemical Technology Co., Ltd. Colloidal silica (30wt% aqueous solution) was purchased from Yuminyuan (Qingdao). Nafion solution (5.0 wt%) was purchased from Sigma-Aldrich. Nafion membranes were purchased from Alfa Aesar. All materials were used directly without further purification. Deionized water was used for all experiments.

2.2. Material synthesis

2.2.1. Synthesis of Cu_xSi catalysts

The Cu_xSi samples were synthesized via a modified Stöber method [22]. Typically, 100 mL of ethanol, 3.2 g of Cu(NO₃)₂·3 H₂O and 12.93 g PVP were added sequentially to a glass vial and ultrasonically dispersed until homogeneous. Then, depending on the copper loading, a certain amount of the obtained solution was added into a glass vial with 150 mL of deionized water and 190 mL of ethanol. After that, 0.552 g CTAB was added into the above solution with constantly magnetic stirring. Then, NH₃·H₂O was added into the solution until pH 11. After 5 min, 1.72 g of tetraethoxysilane (TEOS) was added into the solution drop by drop. The suspension was stirred at room temperature for 48 h. The resulting solid was recovered by filtration and washed with distilled water and ethanol several times to remove CTAB and PVP molecules [23]. Cu_xSi core-shell particle catalysts were obtained after drying the recovered solid in a drying oven at 80 °C for 12 hr.

2.2.2. Synthesis of SiO₂

SiO₂ was prepared using the same method as the Cu_xSi catalysts without adding Cu(NO₃)₂·3 H₂O during the synthesis process.

2.2.3. Synthesis of CuO nanoparticles

CuO nanoparticles were prepared following the same method as the Cu_xSi catalysts without adding TEOS during the synthesis process. The mixture solution obtained through the aforementioned method was heated at 90 °C in an oil bath to facilitate the evaporation of ammonia and the subsequent deposition of CuO nanoparticles at pH 7. The sample was then collected by filtration and washed with distilled water and

ethanol several times. Finally, the sample was dried at 80 °C for 12 h and the CuO nanoparticles were obtained.

2.2.4. Synthesis of CuSiO₃ catalysts

The CuSiO₃ was prepared according to a reported method [24]. Briefly, 2.416 g of Cu(NO₃)₂·3 H₂O and 2.14 g of NH₄Cl were dissolved in 90 mL deionized water. Then, 7.5 mL of NH₃·H₂O was added to the solution to obtain a clear [Cu(NH₃)₄]²⁺ solution. After that, 2.3 g 30 wt % silica sol was added dropwise under magnetic stirring for 30 min. Then the mixture was solvothermally treated at 200 °C for 48 h. The obtained product was centrifuged, washed several times and subsequently dried. Then a calcination process was carried out in a muffle furnace at 400 °C for 4 h, with a heating rate of 2 °C/min. Finally, the calcined CuSiO₃ product was successfully obtained.

2.3. Material characterization

2.3.1. Physical characterization

The X-ray diffraction (XRD) patterns in the 2θ range from 10° to 90° were measured on a Smartlab 8KW equipped with Cu Kα radiation (λ = 1.5406 Å, 60 kV, 220 mA) at a scan rate of 10°/min. The morphology and structure of the catalysts were characterized using field-emission scanning electron microscopy (SEM, Apreo S LoVac) operated at 20 kV and field-emission transmission electron microscopy (TEM, JEOL-2100 F and JEM-F200). Energy dispersive spectroscopy (EDS) elemental mapping was conducted using a JEM-200 field emission transmission electron microscope operated at 200 kV. Fourier transform infrared (FT-IR) spectra of the samples were obtained with a Thermo Fischer Nicolet iS50 spectrometer. The actual concentration of copper in the Cu_xSi catalysts was examined with inductively coupled plasma optical emission spectrometry (ICP-OES, Agilent 5800).

2.3.2. N₂O titration

The N₂O titration is used to determine the copper dispersion by using a VDSorb-91i apparatus. Briefly, a 70 mg sample was first reduced in 10 % H₂/Ar for 1 h at 573 K, then treated by N₂O flow at 363 K to completely oxidized the surface metallic copper to Cu₂O. Finally, the sample was reduced again at 573 K by pulse titration using 10 mol% CO/He. After CO adsorption the sample tube was purged by helium under 100 °C for 60 min. Finally, the temperature was gradually increased to 1000 °C at a rate of 10 °C/min in helium. The vent gas was analyzed by mass spectrometry (MS, Hiden HPR-20 EGA). MID mode was selected as the scanning mode, SEM detector was selected as the detector, and mass-charge ratio was set to 28. The dispersion of CuO species on the catalyst surface were calculated according to the CO desorption amount recorded by the TCD detector, and the formula was as follows:

$$\text{Cu dispersion}(\%) = \frac{MA}{X_{Cu}}$$

where M is the relative atomic molecular mass of Cu (63.546 g/mol);

A is the amount of CO desorption in N₂O-CO TPD (mol/g);

X_{Cu} is the Cu mass fraction measured by ICP-OES.

2.3.3. XAFS measurements and EXAFS analysis

X-ray adsorption fine structure (XAFS) profiles at E₀ = 8979 eV (Cu K-edge) were obtained on XAFS-500-A (Anhui Specreation Instruments Co., Ltd, China). The transmission method was used for measurement, and the scan ranged from 8775 to 9780 eV. All samples were pelletized into disks using cellulose powder as a binder (ground thoroughly by mortar and pestle). The obtained XAFS data was processed by standard procedures via ATHENA module in IFEFFIT software. The EXAFS data was obtained by subtracting the background of post-edge and normalized by the edge jump step. The R-space data was obtained by Fourier transformed by the k-space data. The coordination information can be obtained by the least-squares curve fitting in the R-space using the

ARTEMIS module in IFEFFIT software [25,26].

2.4. Electrochemical measurements

2.4.1. Electrochemical CO₂ reduction reaction

The performance tests were mainly conducted using a typical three-electrode system, with the catalyst-sprayed hydrophobic carbon paper as the working electrode with an effective contact area of $1 \times 1 \text{ cm}^2$. The Pt wire and Ag/AgCl electrode (KCl saturated solution) were used as auxiliary electrode and reference electrode. Electrochemical CO₂ reduction experiments were carried out in a H-type cell with a Nafion 117 proton exchange membrane separating the cathode and anode chambers. The linear sweep voltammetry (LSV) and the potential-dependent CO₂ reduction were both performed in 0.1 M CO₂-saturated KHCO₃ electrolyte (pH 6.8) with continuous gaseous CO₂ flow. All the electrochemical potentials versus Ag/AgCl were converted to that versus reversible hydrogen electrode (RHE) by the following equation:

$$V \text{ vs. RHE} = V \text{ vs. Ag/AgCl} + 0.197 + 0.059 \times \text{pH}$$

Unless otherwise mentioned, “vs. RHE” is omitted for simplicity.

The catalyst ink was prepared by dispersing 10 mg of the prepared catalyst in 5 mL of isopropanol. 10 μL of a 5 wt% Nafion solution was added to the suspension under sonication for 1 h to form a uniform catalyst ink with the catalyst concentration of $2 \text{ mg} \cdot \text{mL}^{-1}$. 400 μL of catalyst ink was sprayed onto a carbon paper. For each electrochemical CO₂ measurement, 30 mL of 0.1 M KHCO₃ electrolyte solutions were utilized in both the anode and cathode chambers of the H-cell. The electrolytes were pre-purged with CO₂ for 15 min before each test. The gas phase products, such as C₂H₄, CH₄, CO and H₂, were detected by online gas chromatograph (GC, Agilent 7890B). The FE for the products can be calculated as follows:

$$FE_i = \frac{n_i \times z_i \times F}{Q} \times 100\%$$

Where n_i is the number of moles of the product (from GC analysis) based on the outlet flow rate (measured with an electronic flow meter);

z_i is the number of electrons required to generate the products ($z=2$ for H₂ and CO, 8 for CH₄, and 12 for C₂H₄);

F is the Faraday's constant (96485 mol/C);

Q is the amount of charge passed during the measurement.

The specific product partial current density was calculated by multiplying the product's FE with the total current density.

2.4.2. In situ ATR-FTIR characterization

In situ ATR-FTIR spectra were acquired with a spectrometer (Thermo Fisher Nicolet IS50) equipped with a mercury-cadmium-telluride (MCT/B) detector and a VeeMAX III ATR accessory (Pike Technologies). A three-electrode spectroelectrochemical cell (Jackfish) was used as the electrolyzer. The catalysts were drop-casted on Gold-sputtered silicon prisms and used as working electrodes. A standard Ag/AgCl electrode and a Pt wire were used as the reference and counter electrodes. A 0.1 M CO₂-saturated KHCO₃-H₂O or KHCO₃-D₂O solution was used as the electrolyte solution. CO₂ with a flow rate of 10 sccm was continually purged during the tests. The electrochemical cell was connected to an electrochemical station and constant potential electrolysis from 0 V to -2.4 V vs. RHE was carried out.

2.4.3. Operando Raman characterization

Operando Raman measurements were carried out with a confocal Raman microscope (LabRAM HR Evolution, Horiba Jobin Yvon) equipped with a 600 grooves/mm diffraction grating. A laser beam with 532 nm wavelength was used as the excitation source without filtering. The grating was calibrated before sample measurements using the first-order peak and the Si lattice peak at 520.7 cm^{-1} of a Si wafer reference sample.

The acquisitions were performed in a self-made 3-electrode Raman electrochemical cell made from PEEK and a quartz window. A leak-free Ag/AgCl electrode and Pt wire were utilized as the reference and counter electrode, respectively. A Cu foil drop-casted with catalyst ink was used as the working electrode. Before signal acquisitions, the laser was focused on the catalyst surface employing a long working distance objective lens (50 times magnification). Raman spectra at all the applied potentials were collected from 400 to 3000 cm^{-1} . During the tests, CO₂ gas was continually bubbled into the 0.1 M KHCO₃ electrolyte and the electrolyte was circulated by a peristaltic pump. The obtained spectra were processed by baseline correction using the Lab solutions 6 software.

2.5. Theoretical calculations

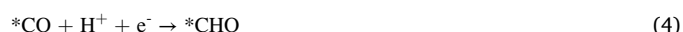
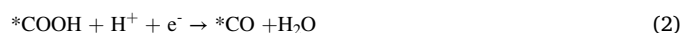
DFT calculations were executed using the Vienna Ab Initio Simulation Package [27,28]. The generalized gradient approximation with the PBE functional and pseudopotential generation in the projector-augmented wave method were employed [29]. Structure relaxation utilized a plane wave basis set with a kinetic energy cutoff of 415 eV and an energy convergence criterion of 10^{-4} eV . An irreducible $3 \times 3 \times 1$ Monkhorst Pack k-point grid was applied. To account for van der Waals interactions, the Grimme's DFT-D3 correction method was systematically incorporated [30]. The climbing image nudged elastic band (CI-NEB) method was adopted to calculate the kinetics barrier of *CO to *CHO process on Cu₁Si and Cu_{0.05}Si. For Cu_xSi catalysts, computational models were crafted by assimilating insights from EXAFS and FT-IR analyses, to discern subtle alterations in Cu-O-Si bond at the interface. The most stable SiO₂ (001) surface was selected. Due to the CO₂RR reaction taking place in a water environment, hydroxyl groups were introduced onto the SiO₂ (001) surface [31]. Different-sized Cu clusters were utilized to represent varying dispersion levels in the Cu_xSi catalysts, with a tetrahedral structure adopted by Cu₄ cluster and a 2 atom – 6 atom – 2 atom structure featured by Cu₁₀ cluster [32]. There were three types of defects in SiO₂, among which NBO defects is considered the most active site. Therefore, NBO defects were introduced onto the SiO₂ catalysts loaded with Cu clusters, in accordance with the rationale derived from earlier research [33]. The Cu (111) and SiO₂(111) substrate was simulated using three layers within a $p(3 \times 3)$ supercell. The top two layers and adsorbates were allowed unrestricted movement in all directions, while the bottom layers remained fixed. To prevent interaction between images, a vertical separation of at least 15 Å was maintained in all cases.

The change in Gibbs free energy (ΔG) for all the reaction steps were calculated based on the method developed by Nørskov et al. [34].

$$\Delta G = \Delta E + \Delta ZPE - T\Delta S$$

where, the ΔE was the energy difference by DFT calculations, ΔZPE was the zero-point energy correction, and ΔS was the vibrational entropy change at room temperature ($T = 298.15 \text{ K}$).

The elementary steps on the catalysts were:



3. Results and discussion

3.1. Material Synthesis and Characterization

Scheme 1 illustrates the synthesis process of copper-silica (Cu_xSi) core-shell catalysts from a modified Stöber method [22,23]. CuO nanoparticles were synthesized from water-in-oil microemulsions using polyvinylpyrrolidone (PVP) and cetyl trimethyl ammonium bromide (CTAB) as co-surfactants. Subsequently, the hydrolysis of tetraethyl orthosilicate (TEOS) formed a continuous layer of silica shell around the CuO nanoparticles. After the removal of surfactant molecules through ethanol extraction, Cu_xSi core-shell catalysts were obtained. By simply adjusting the molar ratio of Cu precursor and TEOS (designated as 'x' in Cu_xSi), CuO nanoparticles of different sizes were formed in the core. For comparison, pure CuO nanoparticles (without silica covering) were also prepared using the same method without the addition of TEOS while pure SiO_2 particles were synthesized by the hydrolysis of TEOS with CTAB and PVP surfactants.

Fig. 1a shows a representative SEM image of a Cu_xSi catalyst ($\text{Cu}_{0.05}\text{Si}$). The Cu_xSi core-shell particle catalysts exhibit a uniform spherical shape with an average size of 359 ± 33 nm (Fig. S1). TEM images (Fig. 1b-c, S2) reveal the Cu_xSi core-shell particle core consists of highly dispersed CuO nanoparticles. The TEM-energy dispersive spectroscopy (EDS) elemental mapping images show the CuO nanoparticles are well located in the core structures of the Cu_xSi particles (Fig. 1d, S3-4).

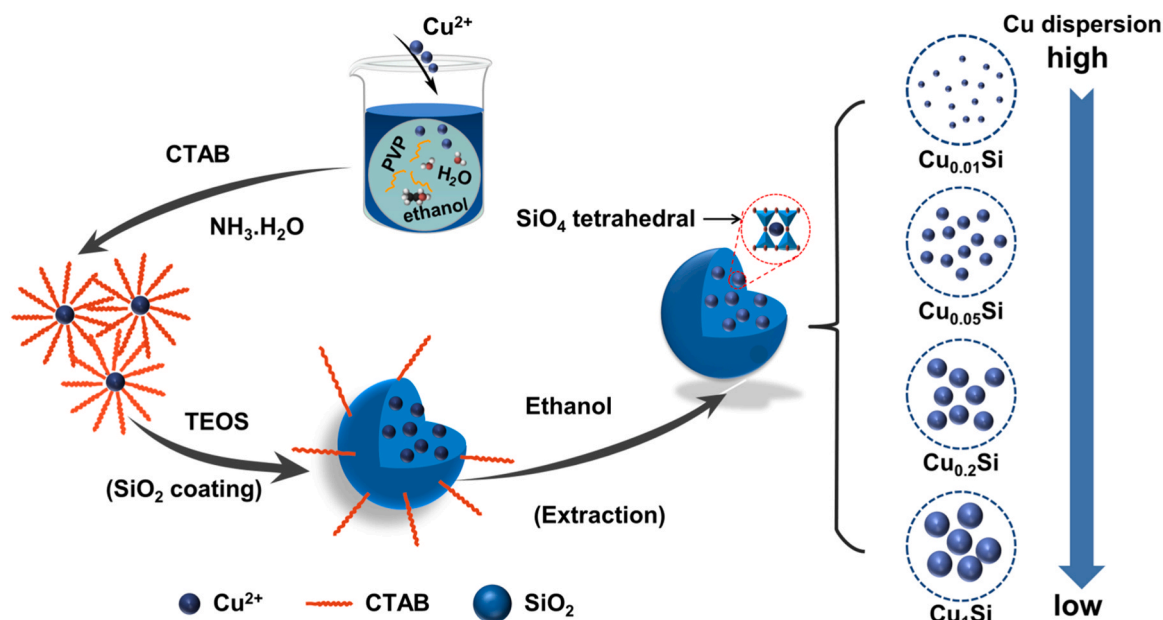
Fig. S2 shows the TEM images and the size histograms of the CuO nanoparticles in the Cu_xSi samples (where $x = 0.01, 0.05, 0.2$ and 1). At a relatively low copper loading, $x = 0.01$, the corresponding size histogram (Fig. S2a) shows the predominance of CuO nanoparticles of ca. 1.5–2.0 nm, with an average value of 1.6 ± 0.3 nm. With an increase in Cu loading, $x = 0.05$ and 0.2 , the average size of the CuO nanoparticles increase to 3.9 ± 0.8 nm and 4.3 ± 0.8 nm, respectively, with a wider range of sizes from 2 to 6.5 nm. Further increase in Cu loading to $x = 1$ results in CuO nanoparticles with a predominance size in the range of 5–8 nm, with an average value of 5.9 ± 1.0 nm. On a whole, from the histograms, it is observed the percentage of larger size CuO nanoparticles increases as the x value (copper loading) increases. This result indicates there is a mixture of CuO nanoparticles in the particle core and the larger CuO nanoparticles are formed due to the growth of smaller

CuO nanoparticles. As the mixture of CuO nanoparticles gets bigger in size as x value increases, these CuO nanoparticles become less dispersed in the core. The percentages of Cu dispersion in the Cu_xSi samples were investigated by N_2O -CO titration (Table S1). The result shows the Cu_xSi catalysts exhibit a copper dispersion of 61.4 % , 35.9 % , 20.6 % and 13.5 % for $x = 0.01, 0.05, 0.2$ and 1 , respectively, and the corresponding actual copper concentration in the Cu_xSi samples, as determined by ICP-OES, are 0.60 wt%, 3.13 wt%, 11.94 wt% and 30.21 wt%, respectively (Table S2).

The crystallinity of the as-synthesized Cu_xSi samples were examined using XRD (Figs. S5–6) as well as TEM. Pure CuO sample shows diffraction peaks at $2\theta = 35.5^\circ$ and 38.7° , which are respectively indexed to the (002) and (111) planes of metallic phase CuO (PDF#45–0937). The pure SiO_2 sample shows only a broad peak at $2\theta = 21.8^\circ$, indicating an amorphous SiO_2 structure. The Cu_xSi samples also show only a similar broad peak at $2\theta = 22.5^\circ$ akin to the peak of SiO_2 sample. The results imply the silica shell deposited around the CuO nanoparticle cores is an amorphous SiO_2 layer. The absence of diffraction peaks associable to a CuO phase indicate the CuO nanoparticles are low in crystallinity. From TEM for Cu_xSi with low copper loading ($x = 0.01$ and 0.05), the representative selected-area electron diffraction (SAED) pattern of the CuO core (inset of Fig. 1b) shows scattered diffuse rings in the corresponding selected-area Fast Fourier Transform (FFT) image (inset of Fig. 1c). This implies the ultrafine CuO nanoparticles (1–4 nm) of $\text{Cu}_{0.01}\text{Si}$ and $\text{Cu}_{0.05}\text{Si}$ exhibit low crystallinity, likely due to the small particle sizes. However, as the CuO particles become larger in size (> 4 nm) in the samples of $\text{Cu}_{0.2}\text{Si}$ and Cu_1Si (Fig. S2i and l), the CuO nanoparticles exhibit clear lattice spacing of 0.232 nm due to improved crystallinity. The lattice spacing of the CuO nanoparticles can be well indexed to a metallic phase CuO (111) facet, in good agreement with XRD results.

To further examine the oxidation state and coordination environments of the Cu_xSi catalysts, X-ray absorption near-edge structure (XANES) and extended X-ray absorption fine structure (EXAFS) are utilized. We performed Cu K-edge XANES with Cu_xSi , along with corresponding reference sample Cu foil, Cu_2O , CuO and CuSiO_3 .

As shown in Fig. 2a, the adsorption edge of Cu_xSi is higher than that of Cu foil and Cu_2O but closer to that of CuSiO_3 and CuO , these features indicate that Cu exists in oxidation state of Cu^{2+} . The Fourier-transform (FT) k^3 -weighted EXAFS spectra for Cu_xSi are presented in Fig. 2b and



Scheme 1. Schematic illustration of Cu_xSi synthesis process.

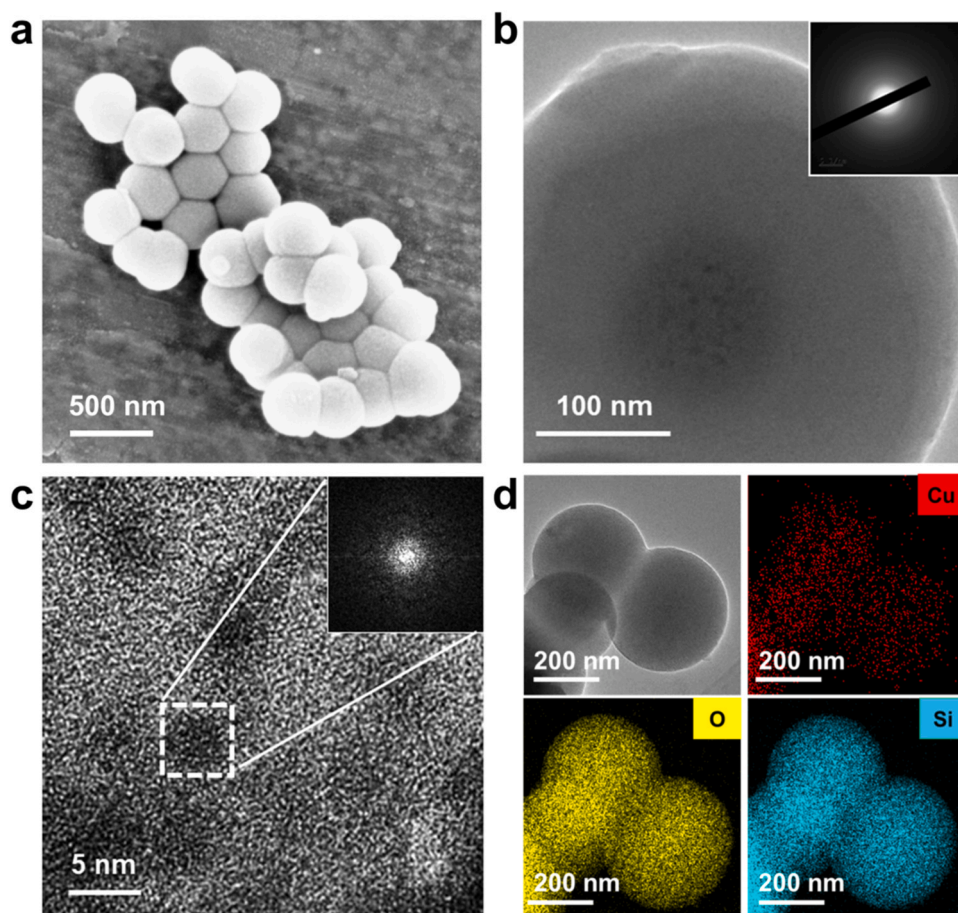


Fig. 1. (a) SEM images of $\text{Cu}_{0.05}\text{Si}$ particle; (b-c) low and high-magnification TEM images of $\text{Cu}_{0.05}\text{Si}$ core-shell particles; the inset image of (b and c) is SAED pattern and corresponding selected-area Fast Fourier Transform image of $\text{Cu}_{0.05}\text{Si}$; (d) TEM image and EDS elemental mapping images of Cu, O, and Si in $\text{Cu}_{0.05}\text{Si}$.

Fig. S7. The spectra of Cu_xSi exhibit a strong peak at $\sim 1.6 \text{ \AA}$, which aligns with the Cu–O bond of CuO ($\sim 1.5 \text{ \AA}$) and CuSiO_3 ($\sim 1.7 \text{ \AA}$) [35]. In addition, the Cu_xSi samples also exhibit a peak at 2.7 \AA . This peak meets well with the Cu–O–Si/Cu–O–Cu bonds of CuSiO_3 (also at 2.7 \AA). These results confirm the dispersion of CuO nanoparticles form Cu–O–Si coordination environment with the SiO_2 shell. To further characterize the Cu–O–Si coordination environment, we performed a wavelet transform (WT)-EXAFS, which can provide a better resolution of EXAFS in k and R space (Fig. 2c and Fig. S8). The Cu_xSi samples exhibit an intense lobe at $\sim 6.0 \text{ \AA}^{-1}$ that matches with the Cu–O coordination of CuO. In addition, a less intense lobe at a slightly higher k , $\sim 8.0 \text{ \AA}^{-1}$, was also observed. This lobe corresponds well with the Cu–O–Si (Cu) coordination of CuSiO_3 and re-affirms the existence of Cu–O–Si coordination. Moreover, EXAFS fitting results indicate the average Cu–O coordination number of Cu_xSi increases as x value increases (Fig. 2d, Fig. S9, Table S3), which implies there are more coordinatively unsaturated Cu atom (relative to the bulk) on Cu_xSi with higher Cu dispersion, which can serve as active sites for CO_2 activation.

3.2. CO_2RR performance

Electrochemical measurements of the obtained samples were conducted in CO_2 -saturated 0.1 M KHCO_3 electrolytes. Linear sweep voltammograms (LSV) shows Cu_xSi produced higher current densities than that of pure CuO and SiO_2 (Fig. 3a and Fig. S10). Among the Cu_xSi catalysts, $\text{Cu}_{0.05}\text{Si}$ exhibits the highest current density of $> 20 \text{ mA cm}^{-2}$ at -2.0 V . Gaseous product measurements using an on-line GC at various CO_2RR potentials indicate $\text{Cu}_{0.05}\text{Si}$ produced CH_4 as the predominant CO_2RR product with CO, C_2H_4 and H_2 as the minor products

(Fig. 3b,c). The $\text{Cu}_{0.05}\text{Si}$ catalyst shows a maximum CH_4 Faradaic efficiency (FE) of 72.9 % at -2.0 V and a CH_4 partial current density of 17.4 mA cm^{-2} (Fig. 3d, S11). Most significantly, compared with other reported materials, $\text{Cu}_{0.05}\text{Si}$ exhibits an exceptionally high CH_4 selectivity (Table S4). The CO_2RR performances of as-obtained Cu_xSi , CuO and SiO_2 catalysts were subsequently compared at -2.0 V (Fig. 3c). CuO produced H_2 (37.3 %), C_2H_4 (24.5 %) and some CH_4 (15.4 %) while SiO_2 produced H_2 mostly. In contrast, the formation of Cu_xSi core-shell particles shifted CO_2RR product selectivity from H_2 to methane and ethylene. Over $\text{Cu}_{0.01}\text{Si}$, which has a relatively low CuO dispersion, a CH_4 selectivity of 27.6 % was obtained. With moderate CuO nanoparticle dispersion in $\text{Cu}_{0.05}\text{Si}$ and $\text{Cu}_{0.2}\text{Si}$, methane was the predominant CO_2RR product from both catalysts at a CH_4 selectivity of 72.9 % and 58.4 %, respectively. However, for Cu_1Si catalyst, which has a low CuO dispersion, the CO_2RR product selectivity shifted from methane to a mixture of methane (16.6 %) and ethylene (30.7 %). The results indicate that the C_1/C_2 selectivity can be regulated through controlling the percentage of CuO nanoparticle dispersion in copper-silica core-shell catalysts (Fig. 3e).

H/D kinetic isotope effect (KIE) measurements are utilized to elucidate the rate-determining step of the CO_2RR process [36,37]. The KIE value is calculated by the ratio of methane formation rates in $\text{KHCO}_3\text{-H}_2\text{O}$ and $\text{KHCO}_3\text{-D}_2\text{O}$. The KIE for CuO, Cu_1Si and $\text{Cu}_{0.05}\text{Si}$ are determined to be 2.27, 1.57 and 1.01, respectively (Fig. 3f). The KIE values for both CuO and Cu_1Si are significantly greater than 1, these imply methane formation on both catalyst is hindered by poor water dissociation rates. In contrast, the KIE value of $\text{Cu}_{0.05}\text{Si}$ catalyst is close to unity, which indicates proton transfer is no longer the rate-determining step for CO_2RR to CH_4 for $\text{Cu}_{0.05}\text{Si}$. The results imply

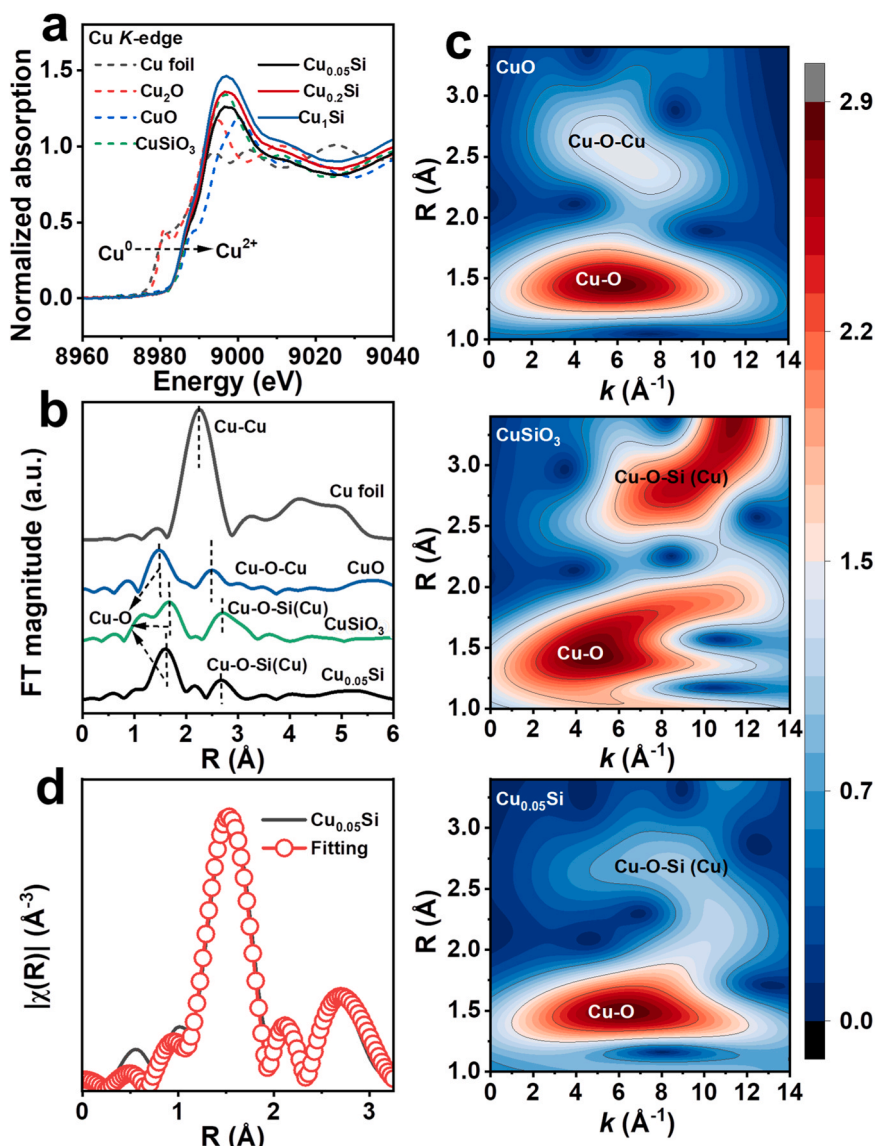


Fig. 2. (a) XANES spectra of the Cu K-edge of the Cu-based catalysts; (b) FT-EXAFS spectra of Cu foil, CuO and Cu_{0.05}Si; (c) Wavelet transforms for the k^3 -weighted EXAFS of CuO, CuSiO₃ and Cu_{0.05}Si; (d) the corresponding EXAFS fitting curve for Cu_{0.05}Si.

water dissociation occurs favorably on Cu_{0.05}Si catalyst, which in turn help in promoting CO₂RR to CH₄ [37].

3.3. Mechanism investigation

To elucidate the CO₂RR mechanism of Cu_xSi catalysts, we employed in situ ATR-IR spectroscopy to identify the reactive species. The electrochemical measurements were conducted in CO₂-saturated 0.1 M KHCO₃ aqueous solutions. As shown in Fig. S12, a band corresponding to Si-H species at 876–885 cm⁻¹ appears in the absorption spectrum of Cu_{0.05}Si while no band is observed in CuO spectra from 750 to 1000 cm⁻¹, indicating that the Cu-O-Si interface demonstrates the capability to provide active proton [21]. Additionally, this Si-H bond is also observed in the *Operando* Raman spectrum (Fig. S13) [38].

Fig. 4a shows the adsorption peaks of intermediates for Cu_{0.05}Si in CO₂RR, the peaks located at 1640 cm⁻¹ and 2110 cm⁻¹ are ascribed to the bending vibration of OH of adsorbed H₂O and the line-bound CO (CO_L), respectively [39]. The transformation of *CO into CH₄ species is indicated by the peaks at 1384, 1473, 1740, 2860, and 2930 cm⁻¹, which are attributed to *OCH₃, *CH₂O, *CHO, -CH₃ symmetric mode and -CH₃ asymmetric mode [40–42]. In fact, the transformation of *CO

to CH₄ appears to follow the path: *CO → *CHO → *CH₂O → *OCH₃ → CH₄. For Cu₁Si catalyst (Fig. 4b), the peak related to the C=O stretching band of the *OCCHO signals at 1587 cm⁻¹ are detected in the in situ ATR-IR test, which indicates Cu₁Si contains active sites for C-C coupling for C₂H₄ synthesis with the proposed mechanism depicted in Figure S14 [41,43]. As illustrated in the schematic diagrams (Fig. 4c), the in situ ATR-IR study reveals that Cu_xSi catalysts with higher Cu dispersion can facilitate the pathway of *CHO successive hydrogenation, while Cu_xSi catalysts with lower Cu dispersion can promote *CHO coupling with *CO to form *OCCHO, thus improving the selectivity of CH₄ or C₂H₄ products during CO₂ reduction, respectively.

We consider the wide O-H bending band of water in the 1700–1550 cm⁻¹ range may overlay with the signal of C=O vibration [39]. To avoid the interference arising from the water peaks, CO₂RR on Cu₁Si was also performed in heavy water D₂O, where O-D bending peak shifts to around 1150 cm⁻¹. As shown in Fig. S15, the band near 1587 cm⁻¹ are still observed, signifying the presence of C=O stretching. These results clearly indicate the formation of the intermediate *OCCHO during CO₂ reduction over Cu₁Si and, therefore confirms Cu₁Si exhibits active sites for C-C coupling to form C₂H₄.

DFT calculations were conducted to further investigate the effects of

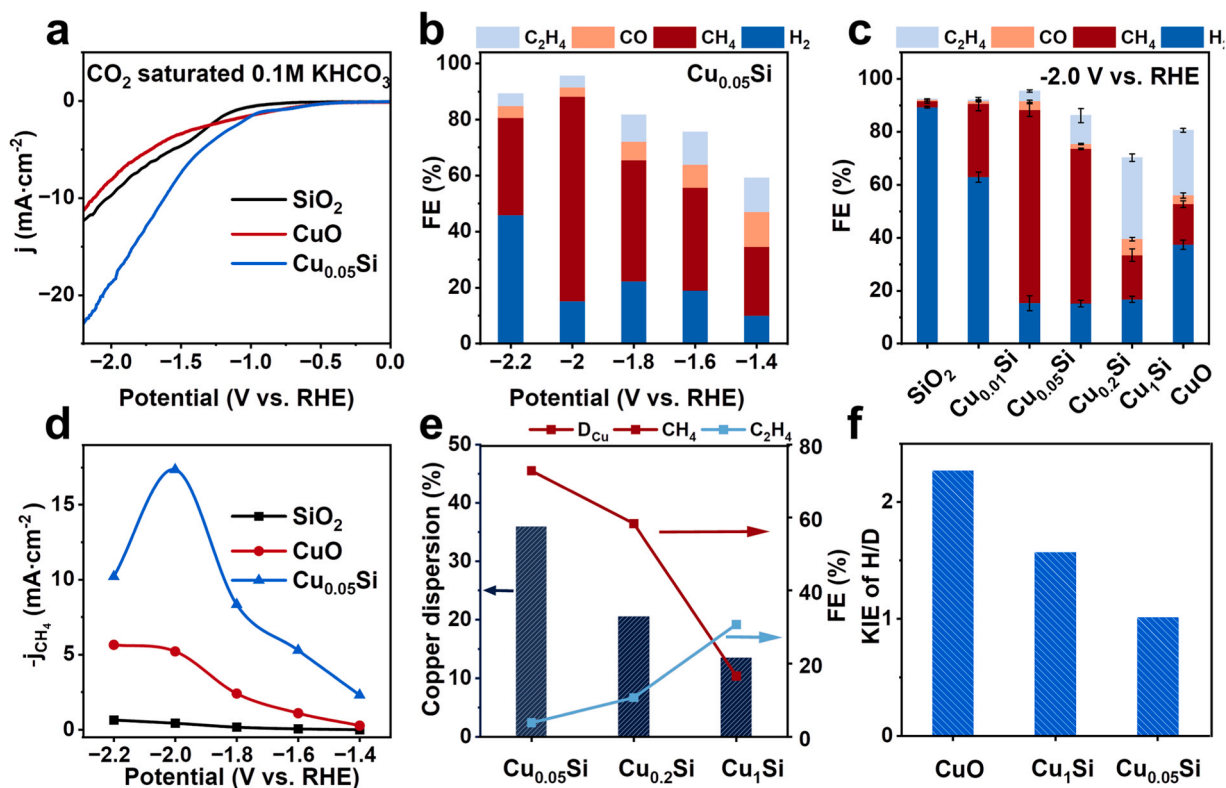


Fig. 3. (a) Linear sweep voltammetry curves of SiO₂, Cu_{0.05}Si, and CuO in CO₂-saturated 0.1 M KHCO₃; (b) FEs at various potentials of Cu_{0.05}Si; (c) FEs at various potentials of SiO₂, Cu_xSi and CuO, all the error bars represent the standard deviation based on three independent measurements; (d) CH₄ partial current density at applied potentials of SiO₂, Cu_{0.05}Si, and CuO; (e) the relationship between the FEs of methane, ethylene and the dispersion of copper; (f) H/D kinetic isotope effect of CuO, Cu₁Si and Cu_{0.05}Si.

different copper dispersion of Cu_xSi catalysts on the coupling of *CO-*CHO and the hydrogenation of *CO to form ethylene and methane, respectively. As CuO undergoes rapid reduction to Cu during the CO₂RR process, the CuO catalyst was simulated using the Cu(111) model [44]. The Cu_{0.05}Si and Cu₁Si were modeled by a Cu₄ cluster and a Cu₁₀ cluster anchored on SiO₂(001) surface, respectively. The detailed computational structure models are presented in Figs. S16 and S17. To clarify the CO₂RR product selectivity for Cu_{0.05}Si and Cu₁Si, the reaction pathways for H₂, CO, CH₄ (*CH_xO) and C₂H₄ (*OCCHO) were considered [45,46]. As for the H₂ pathway, the Gibbs free energy of Cu_{0.05}Si (1.16 eV) and Cu₁Si (1.69 eV) are relatively high, demonstrating that the Cu_xSi catalysts inhibit the competing HER effectively (Fig. S18). For the CO pathway, the desorption energy of *CO from the Cu_xSi catalysts are higher than the energy barrier for the *CO → *CHO transition, making the reaction more likely to proceed along the *CO → *CHO pathway (Fig. 5a and b). For the CO₂RR, the hydrogenation of *CO to *CH_xO (x = 1, 2, or 3) is considered a pivotal reaction step determining the selectivity towards CH₄ while *CO-*CHO coupling plays a critical role in the generation of C₂H₄ [13,47]. Hence, the Gibbs free energy and the kinetics barrier for the hydrogenation of *CO to *CHO was computed through DFT, revealing that on Cu_{0.05}Si and Cu₁Si catalysts, the energy barrier for *CO hydrogenation to *CHO is lower than that on CuO (Fig. S19). The transition-state (TS) energy barriers for the hydrogenation of *CO to *CHO for CuO, Cu_{0.05}Si and Cu₁Si are 1.19 eV, 0.76 eV and 1.13 eV, respectively. This can be attributed to the observation that on CuO, *CHO predominantly adsorbs through C atom at Cu fcc sites, whereas on Cu_xSi catalysts, *CHO adsorbs with C atom on the Cu-O-Si bond and O atom on Cu atom. The Cu-O-Si structure stabilizes the adsorption of the intermediate *CHO, facilitating the hydrogenation of *CO to *CHO. To further discern the reaction pathways of Cu_xSi catalysts with varying Cu concentrations, the Gibbs free energy for the hydrogenation of *CHO to *CH₂O is calculated. The Gibbs free energy

diagram in Fig. 5a indicate the energy barrier for Cu_{0.05}Si catalyst to produce *CH₂O is -1.28 eV, which is lower than the barrier for producing *OCCHO (-0.40 eV), suggesting a greater ease for CH₄ formation than C₂H₄. However, for Cu₁Si catalyst, the energy barrier for producing *OCCHO is lower than that for forming *CH₂O (Fig. 5b). Therefore, C₂H₄ formation is observed for Cu₁Si catalyst.

We computed the Cu 3d partial density of states (PDOS) to obtain more insights into the electronic properties of Cu_{0.05}Si and Cu₁Si. Attributed to the formation of higher-lying Cu d_{z2}, d_{xz}, and d_{yz} orbitals, the Cu d-band center of Cu₁Si catalyst (-1.45 eV, Fig. 5d) is observed to be closer to the Fermi level than that of Cu_{0.05}Si catalyst (-1.79 eV, Fig. 5c). The ability for Cu₁Si to support C-C coupling and produce C₂H₄ can be explained by the elevated energy levels of Cu d_{z2}, d_{xz}, and d_{yz} orbitals, which help enhance the electron accepting ability of Cu atoms [48]. The "donor-acceptor" mechanism of electrons plays a crucial role in understanding the DOS [49]. We further computed Bader charges and differential charges (Fig. S20) for the Cu_xSi, which show for Cu₁Si, Cu loses 0.50 e/atom while for Cu_{0.05}Si, Cu loses 0.76 e/atom. Therefore, the electron transfer between Cu and SiO₂ is stronger in Cu_{0.05}Si than Cu₁Si. Cu donates electrons to the O atoms in SiO₂, which explains why the partial occupancy of d_{z2}, d_{xz}, and d_{yz} orbitals decreases in Cu_{0.05}Si, and the center of the d-band moves away from the Fermi level.

The adsorption strength of *CHO intermediates were also evaluated at the Cu-O-Si interface. In comparison to Cu₁Si catalyst, the PDOS of *CHO on Cu_{0.05}Si catalyst exhibits a noticeable weakening of the 2π* orbital, indicating enhanced feedback interactions from the Cu-O-Si interface to the *CHO [50]. This results in a reduction of the C-O bond order, suggesting that the Cu-O-Si surface adsorption activates the C-O bond, making it more prone for *CHO to undergo deeper hydrogenation to *CH₂O (Fig. 5e and f). The splitting of the 5σ orbitals is more pronounced, with the orbitals shifting to lower energy levels, implying that *CHO is more easily hydrogenated and desorbed on the Cu_{0.05}Si

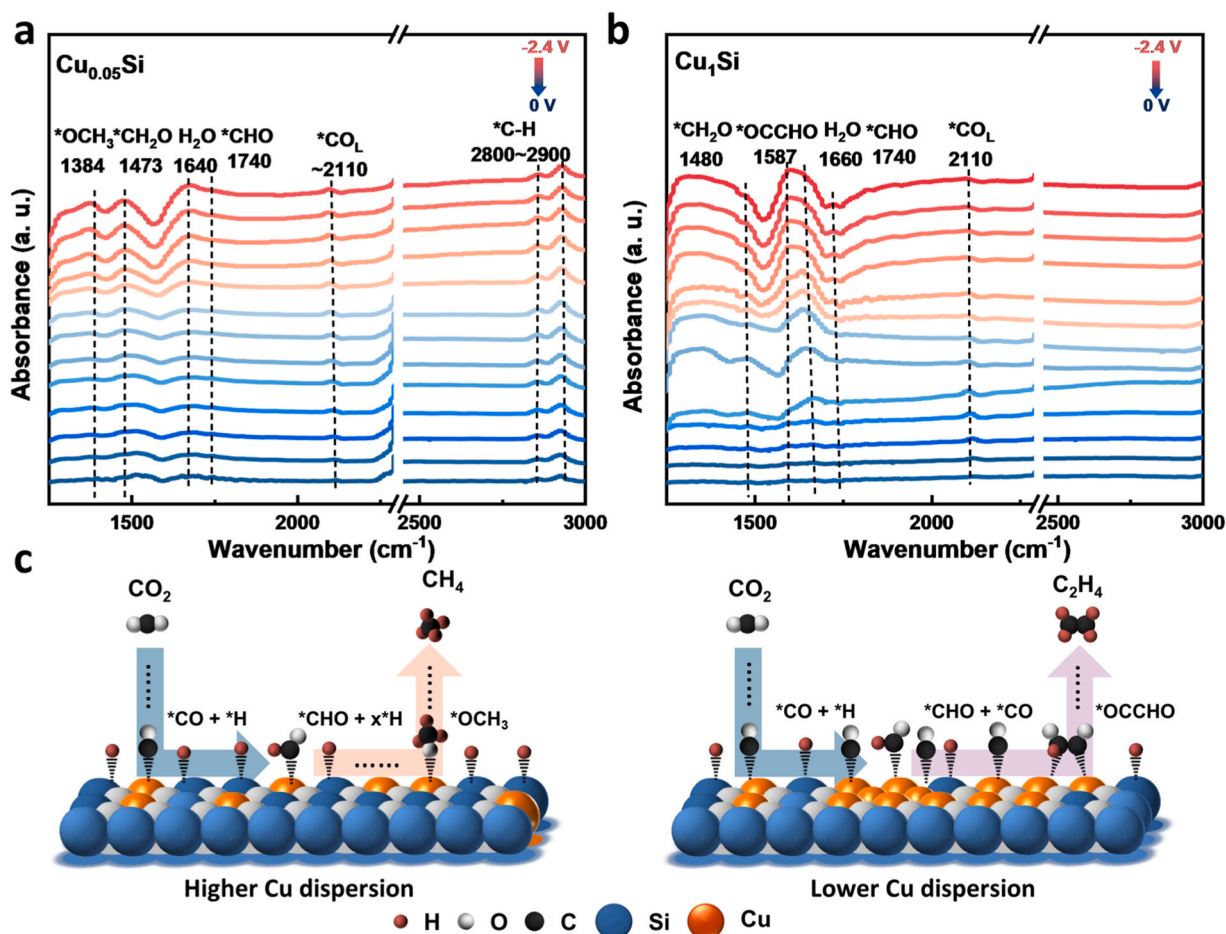


Fig. 4. In situ ATR-FTIR of (a) $\text{Cu}_{0.05}\text{Si}$ and (b) Cu_1Si in CO_2 -saturated 0.1 M KHCO_3 ; (c) schematic illustrations of the proposed reaction mechanism of CO_2RR to CH_4 or C_2H_4 on the Cu_xSi catalysts with different Cu dispersion.

catalyst.

Water dissociation serves as a pivotal source of $^*\text{H}$ in the CO_2RR process. Promotion of water dissociation can substantially enhance CO_2RR activity [36]. To elucidate the origin of the strong water dissociation ability of $\text{Cu}_{0.05}\text{Si}$ leading to the high methane selectivity, we examine the Gibbs free energy for H_2O dissociation on CuO , $\text{Cu}_{0.05}\text{Si}$ and Cu_1Si catalysts. We observe $\text{Cu}_{0.05}\text{Si}$ with an appropriately added amount of Cu manifests a significantly reduced Gibbs free energy for water dissociation (-0.94 eV) compared to CuO (-0.22 eV) and Cu_1Si (-0.29 eV) (Fig. 6a). This reduction is ascribed to the capacity for the added Cu to form exposed Cu-O-Si interfaces, water dissociation on the Cu-O-Si site is highly favorable. However, for Cu_1Si , the excessive Cu coverage conceals the Si-O structure and limits the exposure of Cu-O-Si interfaces for water activation. Further calculations were performed to examine the adsorption energy of $^*\text{H}$ on Cu_xSi and CuO catalysts, revealing that $\text{Cu}_{0.05}\text{Si}$ exhibits stronger $^*\text{H}$ adsorption (-6.78 eV) compared to CuO (-3.42 eV) and Cu_1Si (-5.41 eV) (Table S5). The results imply the surface coverage of reactive $^*\text{H}$ is highest on $\text{Cu}_{0.05}\text{Si}$ upon biasing. The hydrogenation rates of $^*\text{CO}$ can be expected to increase when surface adsorbed $^*\text{CO}$ react actively with the populated $^*\text{H}$ on $\text{Cu}_{0.05}\text{Si}$ catalyst to form methane.

To further analyze the water dissociation process, we examine the possible configurations for a water molecule to adsorb and dissociate on the catalysts. The most possible configurations are illustrated in Fig. 6b. For CuO , the O atom of water molecule (O_w) adsorbs on the Cu top site. For $\text{Cu}_{0.05}\text{Si}$, O_w adsorbs on the Cu-Si bridge site while for Cu_1Si , where the Cu-Si bridge site is inaccessible for water adsorption, O_w adsorbs on the Cu top site. For Cu_xSi , we observe the adsorbed H_2O molecules form

hydrogen bonding network with SiO_2 , which aids in stabilizing the H atoms of H_2O molecules [51]. Notably, the variation in adsorption sites on the catalysts results in discernible differences in the O-H bond length of water. The O-H bond length is longest on $\text{Cu}_{0.05}\text{Si}$ (1.10 Å), follows by Cu_1Si (1.01 Å) and CuO (0.98 Å). Lengthening of O-H bond length in H_2O suggests a greater likelihood for its dissociation. Therefore, water is most ready to dissociate in the order of $\text{Cu}_{0.05}\text{Si} > \text{Cu}_1\text{Si} > \text{CuO}$.

The PDOS of O_w 2p, Cu 3d and Si 2p orbitals for water adsorbed CuO and Cu_xSi are constructed to help clarify the reaction mechanisms (Fig. 6c). The $1b_2$ orbital is the primary bonding orbital for the O-H bond in H_2O while the $3a_1$ and $1b_1$ orbitals comprise the lone pair electrons of O_w . Characteristic variations in these orbitals offer useful insights into the changes in the density of states of H_2O across the catalysts. Compared to CuO and Cu_1Si , the $1b_2$ orbital of O_w on $\text{Cu}_{0.05}\text{Si}$ is the farthest from the H 1s orbital. This indicates the interaction between H and O in H_2O is the weakest on $\text{Cu}_{0.05}\text{Si}$ (i.e., the O-H bond is most likely to break). In addition, the strong hybridization between Si 2p and O_w $1b_1$ orbital results in an increased electron density in O_w $1b_1$ orbital state, which in turn helps water activation [51].

Based on the DFT calculations, we conclude two factors contributing to the elevated methane selectivity of $\text{Cu}_{0.05}\text{Si}$. Firstly, in comparison to the less Cu dispersed Cu_1Si , the $^*\text{CHO}$ intermediate on the high Cu dispersed $\text{Cu}_{0.05}\text{Si}$ tends to undergo hydrogenation rather than C-C coupling, which helps in methane formation. Secondly, the higher dispersion of Cu nanoparticles in $\text{Cu}_{0.05}\text{Si}$ enables the formation of a larger number of exposed Cu-O-Si sites. These Cu-O-Si interfaces facilitate water dissociation, providing more protons for the $^*\text{CHO}$ hydrogenation process.

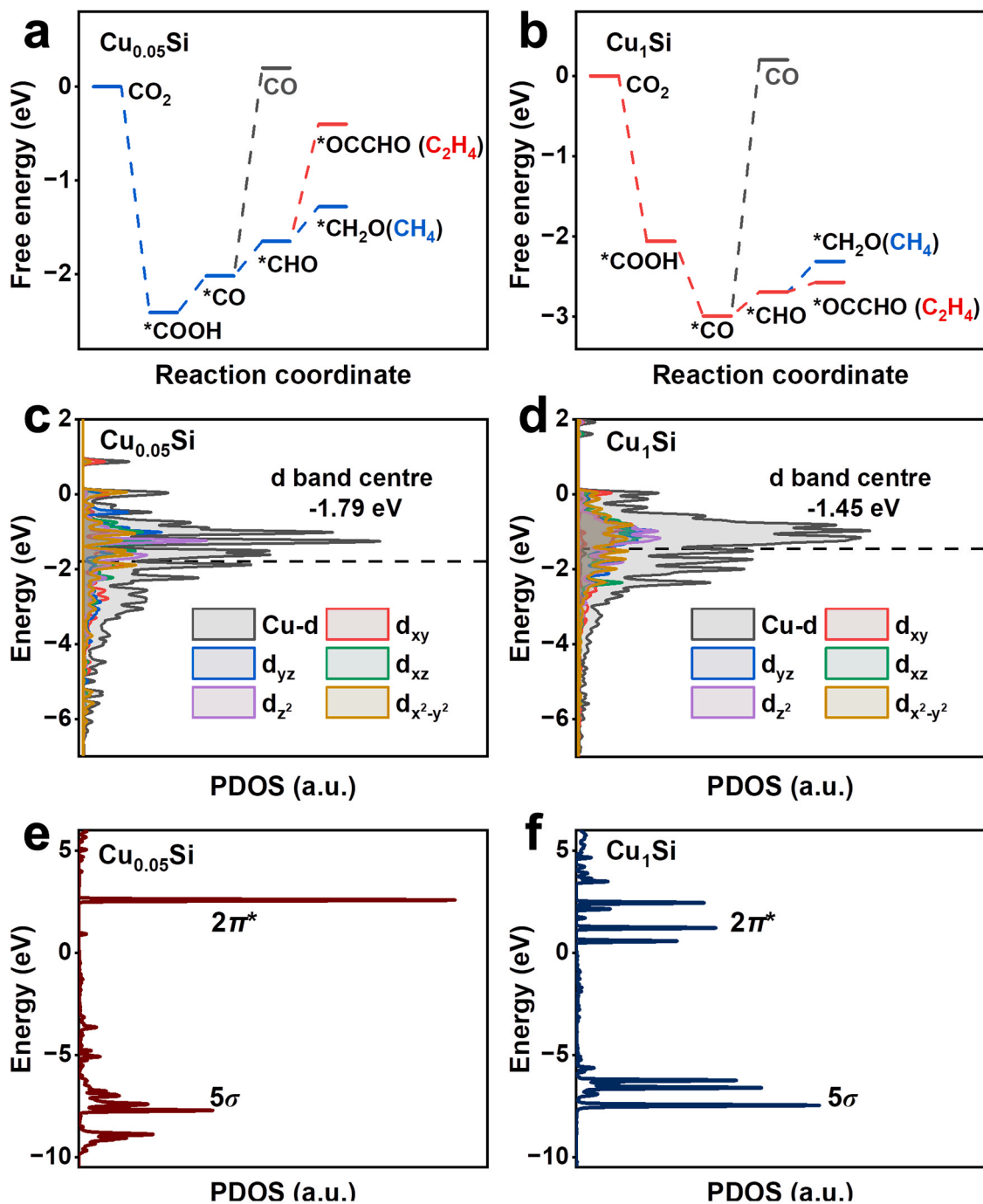


Fig. 5. Gibbs free energy of CO₂ reduction to CO, CH₄ (*CH₂O) and C₂H₄ (*OCCHO) via various pathways on (a) Cu_{0.05}Si and (b) Cu₁Si; the Cu 3d PDOS and ORDOS on (c) Cu_{0.05}Si and (d) Cu₁Si, black lines: d-band centre; the PDOS onto the s and p states of *CHO on (e) Cu_{0.05}Si and (f) Cu₁Si.

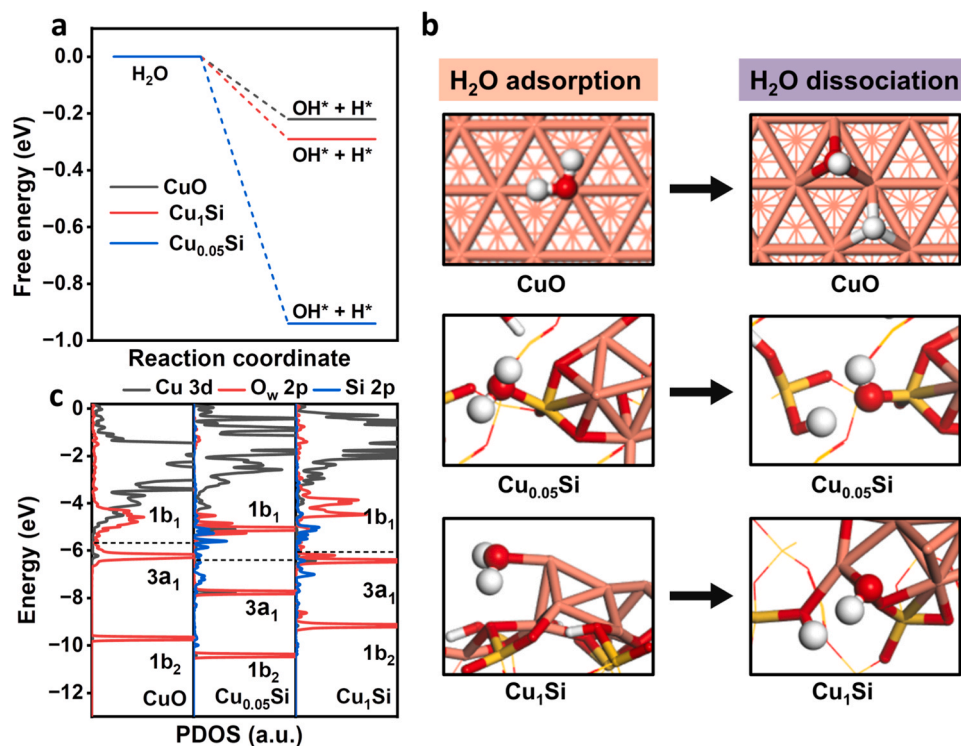


Fig. 6. (a) Gibbs free energy of the H₂O dissociation on CuO, Cu_{0.05}Si and Cu₁Si; (b) The configuration of the H₂O adsorption and dissociation on CuO, Cu_{0.05}Si, and Cu₁Si, color-code atoms represent Cu (pink), Si (yellow), O (red), H (white); (c) the O_w 2p PDOS on CuO, Cu_{0.05}Si, and Cu₁Si, black lines: p-band centre.

4. Conclusions

In summary, core-shell Cu_xSi catalysts with varied copper dispersions were carefully fabricated through a modified Stöber method. The introduction of SiO₂ could provide abundant *H species to help with the successive hydrogenation of *CO. The fine-tuned Cu dispersion on silica create abundant Cu-O-Si sites with reduced energy barriers for both water dissociation and hydrogenation of *CO. The Cu_{0.05}Si catalyst with moderate Cu dispersion forms *CH_xO favorably, resulting in an outstanding CH₄ selectivity of 72.9 %. On the other hand, a lower Cu dispersion on silica forms *OCCHO more favorably, leading to C₂H₄ formation. This study provides fresh insights into Cu-O-Si interface for water dissociation and *CO hydrogenation, which may invoke new strategy for the rational design of efficient electrocatalysts for CO₂ reduction.

CRediT authorship contribution statement

Sheng Zhang: Writing – review & editing, Supervision, Resources, Funding acquisition, Conceptualization. **Xinbin Ma:** Supervision, Resources, Conceptualization, Writing – review & editing. **Jianlong Lin:** Investigation. **Siyu Kuang:** Investigation. **Tiantian Xiao:** Formal analysis, Methodology. **Zhihui Liu:** Methodology, Investigation. **Tianxiang Yan:** Investigation, Methodology. **Yaxin Jin:** Writing – original draft, Methodology, Formal analysis. **Shi Nee Lou:** Writing – review & editing, Supervision, Methodology, Funding acquisition, Conceptualization. **Tianying Zhang:** Writing – original draft, Methodology, Investigation, Conceptualization.

Declaration of Competing Interest

The authors declare that they have no known competing financial interests or personal relationships that could have appeared to influence the work reported in this paper.

Data Availability

Data will be made available on request.

Acknowledgements

The authors are grateful for the financial support from National Key Research and Development Program of China (Grant No. 2023YFA1507901, and 2022YFB4101702), National Nature Science Foundation of China (Grant No. 22078232, 21938008, and 22250410262), and Tianjin Science and Technology Bureau Applied Basic Program Surface Project (Grant No. 22JCYBJC01410).

Appendix A. Supporting information

Supplementary data associated with this article can be found in the online version at [doi:10.1016/j.apcatb.2024.124065](https://doi.org/10.1016/j.apcatb.2024.124065).

References

- [1] T. Yan, X. Chen, L. Kumari, J. Lin, M. Li, Q. Fan, H. Chi, T.J. Meyer, S. Zhang, X. Ma, Multiscale CO₂ electrocatalysis to C₂₊ products: reaction mechanisms, catalyst design, and device fabrication, *Chem. Rev.* 123 (2023) 10530–10583, <https://doi.org/10.1021/acs.chemrev.2c00514>.
- [2] Q. Fan, G. Bao, X. Chen, Y. Meng, S. Zhang, X. Ma, Iron nanoparticles tuned to catalyze CO₂ electroreduction in acidic solutions through chemical microenvironment engineering, *ACS Catal.* 12 (2022) 7517–7523, <https://doi.org/10.1021/acscatal.2c01890>.
- [3] S. Yan, C. Peng, C. Yang, Y. Chen, J. Zhang, A. Guan, X. Lv, H. Wang, Z. Wang, T.-K. Sham, Q. Han, G. Zheng, Electron localization and lattice strain induced by surface lithium doping enable ampere-level electrosynthesis of formate from CO₂, *Angew. Chem. Int. Ed.* 60 (2021) 25741–25745, <https://doi.org/10.1002/anie.202111351>.
- [4] S. Liang, T. Zhang, Y. Zheng, T. Xue, Z. Wang, Q. Wang, H. He, Maximizing the utilization of single-atom sites on carbon-based catalysts for efficient CO₂ electroreduction with ultrahigh turnover frequency, *Appl. Catal., B* 333 (2023), <https://doi.org/10.1016/j.apcatb.2023.122801>.
- [5] W. Lai, Y. Qiao, Y. Wang, H. Huang, Stability issues in electrochemical CO₂ reduction: recent advances in fundamental understanding and design strategies, *Adv. Mater.* 35 (2023) e2306288, <https://doi.org/10.1002/adma.202306288>.

- [6] D. Gao, W. Li, H. Wang, G. Wang, R. Cai, Heterogeneous catalysis for CO₂ conversion into chemicals and fuels, *Trans. Tianjin Univ.* 28 (2022) 245–264, <https://doi.org/10.1007/s12209-022-00326-x>.
- [7] S. Kuang, T. Xiao, H. Chi, J. Liu, C. Mu, H. Liu, S. Wang, Y. Yu, T.J. Meyer, S. Zhang, X. Ma, Acetamide electrosynthesis from CO₂ and nitrite in water, *Angew. Chem. Int. Ed.* 63 (2024) e202316772, <https://doi.org/10.1002/anie.202316772>.
- [8] J. Zhang, G. Zeng, S. Zhu, H. Tao, Y. Pan, W. Lai, J. Bao, C. Lian, D. Su, M. Shao, H. Huang, Steering CO₂ electroreduction pathway toward ethanol via surface-bounded hydroxyl species-induced noncovalent interaction, *Proc. Natl. Acad. Sci. U. S. A.* 120 (2023) e2218987120, <https://doi.org/10.1073/pnas.2218987120>.
- [9] J. Liu, Q. Fan, X. Chen, S. Kuang, T. Yan, H. Liu, S. Zhang, X. Ma, Hollow copper nanocubes promoting CO₂ electroreduction to multicarbon products, *Ind. Eng. Chem. Res.* 61 (2022) 18250–18257, <https://doi.org/10.1021/acs.iecr.2c03912>.
- [10] S. Kuang, M. Li, R. Xia, L. Xing, Y. Su, Q. Fan, J. Liu, E.J.M. Hensen, X. Ma, S. Zhang, Stable surface-anchored Cu nanocubes for CO₂ electroreduction to ethylene, *ACS Appl. Nano Mater.* 3 (2020) 8328–8334, <https://doi.org/10.1021/acsnanm.0c01745>.
- [11] L. Lv, X. He, J. Wang, Y. Ruan, S. Ouyang, H. Yuan, T. Zhang, Charge localization to optimize reactant adsorption on KCu₂S₄/CuO interfacial structure toward selective CO₂ electroreduction, *Appl. Catal., B* 298 (2021), <https://doi.org/10.1016/j.apcatb.2021.120531>.
- [12] W.F. Xiong, D.H. Si, H.F. Li, X. Song, T. Wang, Y.B. Huang, T.F. Liu, T. Zhang, R. Cao, Steering CO₂ electroreduction selectivity U-turn to ethylene by Cu-Si bonded interface, *J. Am. Chem. Soc.* 146 (2024) 289–297, <https://doi.org/10.1021/jacs.3c08867>.
- [13] J. Li, A. Ozden, M. Wan, Y. Hu, F. Li, Y. Wang, R.R. Zamani, D. Ren, Z. Wang, Y. Xu, D.-H. Nam, J. Wicks, B. Chen, X. Wang, M. Luo, M. Graetzel, F. Che, E.H. Sargent, D. Sinton, Silica-copper catalyst interfaces enable carbon-carbon coupling towards ethylene electrosynthesis, *Nat. Commun.* 12 (2021), <https://doi.org/10.1038/s41467-021-23023-0>.
- [14] D. Wang, L. Li, Q. Xia, S. Hong, L. Hao, A.W. Robertson, Z. Sun, Boosting CO₂ electroreduction to multicarbon products via tuning of the copper surface charge, *ACS Sustain. Chem. Eng.* 10 (2022) 11451–11458, <https://doi.org/10.1021/acssuschemeng.2c03963>.
- [15] X. Tan, K. Sun, Z. Zhuang, B. Hu, Y. Zhang, Q. Liu, C. He, Z. Xu, C. Chen, H. Xiao, C. Chen, Stabilizing copper by a reconstruction-resistant atomic Cu-O-Si interface for electrochemical CO₂ reduction, *J. Am. Chem. Soc.* 145 (2023) 8656–8664, <https://doi.org/10.1021/jacs.3c01638>.
- [16] X. Yuan, S. Chen, D. Cheng, L. Li, W. Zhu, D. Zhong, Z.-J. Zhao, J. Li, T. Wang, J. Gong, Controllable Cu-O-Cu⁺ sites for electrocatalytic reduction of carbon dioxide, *Angew. Chem. Int. Ed.* 60 (2021) 15344–15347, <https://doi.org/10.1002/anie.202105118>.
- [17] Q. Li, J. Wu, L. Lv, L. Zheng, Q. Zheng, S. Li, C. Yang, C. Long, S. Chen, Z. Tang, Efficient CO₂ electroreduction to multicarbon products at CuSiO₃/CuO derived interfaces in ordered pores, *Adv. Mater.* (2023) e2305508, <https://doi.org/10.1002/adma.202305508>.
- [18] Z. Yang, X. Wen, X. Guo, Y. Chen, R. Wei, L. Gao, X. Pan, J. Zhang, G. Xiao, High dispersion dendritic fibrous morphology nanospheres for electrochemical CO₂ reduction to C₂H₄, *J. Colloid Interface Sci.* 650 (2023) 1446–1456, <https://doi.org/10.1016/j.jcis.2023.07.118>.
- [19] C. Xu, G. Chen, Y. Zhao, P. Liu, X. Duan, L. Gu, G. Fu, Y. Yuan, N. Zheng, Interfacing with silica boosts the catalysis of copper, *Nat. Commun.* 9 (2018), <https://doi.org/10.1038/s41467-018-05757-6>.
- [20] J. Gong, H. Yue, Y. Zhao, S. Zhao, L. Zhao, J. Lv, S. Wang, X. Ma, Synthesis of ethanol via syngas on Cu/SiO₂ catalysts with balanced Cu-O-Cu⁺ sites, *J. Am. Chem. Soc.* 134 (2012) 13922–13925, <https://doi.org/10.1021/ja3034153>.
- [21] A.K. Mishra, R. Belgamwar, R. Jana, A. Datta, V. Polshettiwar, Defects in nanosilica catalytically convert CO₂ to methane without any metal and ligand, *Proc. Natl. Acad. Sci. U. S. A.* 117 (2020) 6383–6390, <https://doi.org/10.1073/pnas.1917237117>.
- [22] H. Yang, Y. Chen, X. Cui, G. Wang, Y. Cen, T. Deng, W. Yan, J. Gao, S. Zhu, U. Olsbye, J. Wang, W. Fan, A highly stable copper-based catalyst for clarifying the catalytic roles of Cu⁰ and Cu⁺ species in methanol dehydrogenation, *Angew. Chem. Int. Ed. Engl.* 57 (2018) 1836–1840, <https://doi.org/10.1002/anie.201710605>.
- [23] Q. Yue, Y. Zhang, Y. Jiang, J. Li, H. Zhang, C. Yu, A.A. Elzathary, A. Alghamdi, Y. Deng, D. Zhao, Nanoengineering of Core-Shell magnetic mesoporous microspheres with tunable surface roughness, *J. Am. Chem. Soc.* 139 (2017) 4954–4961, <https://doi.org/10.1021/jacs.7b01464>.
- [24] H. Wang, W. Zhao, M.U. Rehman, W. Liu, Y. Xu, H. Huang, S. Wang, Y. Zhao, D. Mei, X. Ma, Copper phyllosilicate nanotube catalysts for the chemosynthesis of cyclohexane via hydrodeoxygenation of phenol, *ACS Catal.* 12 (2022) 4724–4736, <https://doi.org/10.1021/acscatal.2c00380>.
- [25] H. Funke, M. Chukalina, A. Rossberg, Wavelet analysis of extended x-ray absorption fine structure data, *Phys. Scr.* T115 (2005) 232–234, <https://doi.org/10.1238/physica.topical.115a00232>.
- [26] H. Funke, M. Chukalina, A.C. Scheinost, A new FEFF-based wavelet for EXAFS data analysis, *J. Synchrotron Radiat.* 14 (2007) 426–432, <https://doi.org/10.1107/s0909049507031901>.
- [27] G. Kresse, J. Hafner, Ab initio molecular dynamics for liquid metals, *Phys. Rev. B* 47 (1993) 558–561, <https://doi.org/10.1103/physrevb.47.558>.
- [28] P.E. Blochl, Projector augmented-wave method, *Phys. Rev. B* 50 (1994) 17953–17979, <https://doi.org/10.1103/physrevb.50.17953>.
- [29] J.P. Perdew, K. Burke, M. Ernzerhof, Generalized gradient approximation made simple, *Phys. Rev. Lett.* 77 (1996) 3865, <https://doi.org/10.1103/physrevlett.77.3865>.
- [30] S. Grimme, Semiempirical gga-type density functional constructed with a long-range dispersion correction, *J. Comput. Chem.* 27 (2006) 1787–1799, <https://doi.org/10.1002/jcc.20495>.
- [31] Z. Cheng, H. Shan, Y. Sun, L. Zhang, H. Jiang, C. Li, Evolution mechanism of surface hydroxyl groups of silica during heat treatment, *Appl. Surf. Sci.* 513 (2020), <https://doi.org/10.1016/j.apsusc.2020.145766>.
- [32] P. Schlexer, H.-Y.T. Chen, G. Pacchioni, CO₂ activation and hydrogenation: A comparative DFT study of Ru₁₀/TiO₂ and Cu₁₀/TiO₂ model catalysts, *Catal. Lett.* 147 (2017) 1871–1881, <https://doi.org/10.1007/s10562-017-2098-1>.
- [33] Nuria Lopez, Francesc Illas, Gianfranco Pacchioni, Ab initio theory of metal deposition on SiO₂. 1. Cu_n (n = 1–5) clusters on nonbridging oxygen defects, *J. Phys. Chem. B* 103 (1999) 1712–1718, <https://doi.org/10.1021/jp9840174>.
- [34] J.K. Nørskov, J. Rossmeisl, A. Logadottir, L. Lindqvist, J.R. Kitchin, T. Bligaard, H. Jonsson, Origin of the overpotential for oxygen reduction at a fuel-cell cathode, *J. Phys. Chem. B* 108 (2004) 17886–17892, <https://doi.org/10.1021/jp047349j>.
- [35] H. Bao, Y. Qiu, X. Peng, J.A. Wang, Y. Mi, S. Zhao, X. Liu, Y. Liu, R. Cao, L. Zhuo, J. Ren, J. Sun, J. Luo, X. Sun, Isolated copper single sites for high-performance electroreduction of carbon monoxide to multicarbon products, *Nat. Commun.* 12 (2021) 238, <https://doi.org/10.1038/s41467-020-20336-4>.
- [36] H. Liu, B. Li, Z. Liu, Z. Liang, H. Chuai, H. Wang, S.N. Lou, Y. Su, S. Zhang, X. Ma, Ceria-mediated dynamic Sn⁰/Sn²⁺ redox cycle for CO₂ electroreduction, *ACS Catal.* 13 (2023) 5033–5042, <https://doi.org/10.1021/acscatal.2c06135>.
- [37] W. Ma, S. Xie, T. Liu, Q. Fan, J. Ye, F. Sun, Z. Jiang, Q. Zhang, J. Cheng, Y. Wang, Electrocatalytic reduction of CO₂ to ethylene and ethanol through hydrogen-assisted C-C coupling over fluorine-modified copper, *Nat. Catal.* 3 (2020) 478–487, <https://doi.org/10.1038/s41929-020-0450-0>.
- [38] Y. Ma, Y.L. Huang, R. Job, W.R. Fahrner, Dissociation, transformation, and recombination of Si-H bonds in hydrogenated crystalline silicon determined by in situ micro-Raman spectroscopy, *Phys. Rev. B* 71 (2005), <https://doi.org/10.1103/PhysRevB.71.045206>.
- [39] S. Kuang, Y. Su, M. Li, H. Liu, H. Chuai, X. Chen, E.J.M. Hensen, T.J. Meyer, S. Zhang, X. Ma, Asymmetrical electrohydrogenation of CO₂ to ethanol with copper-gold heterojunctions, e2214175120, *Proc. Natl. Acad. Sci. U. S. A.* 120 (2023) e2214175120, <https://doi.org/10.1073/pnas.2214175120>.
- [40] X. Xie, X. Zhang, M. Xie, L. Xiong, H. Sun, Y. Lu, Q. Mu, M.H. Rummeli, J. Xu, S. Li, J. Zhong, Z. Deng, B. Ma, T. Cheng, W.A. Goddard 3rd, Y. Peng, Au-activated n motifs in non-coherent cupric porphyrin metal organic frameworks for promoting and stabilizing ethylene production, *Nat. Commun.* 13 (2022) 63, <https://doi.org/10.1038/s41467-021-27768-6>.
- [41] G. Feng, S. Wang, S. Li, R. Ge, X. Feng, J. Zhang, Y. Song, X. Dong, J. Zhang, G. Zeng, Q. Zhang, G. Ma, Y.D. Chuang, X. Zhang, J. Guo, Y. Sun, W. Wei, W. Chen, Highly selective photoelectroreduction of carbon dioxide to ethanol over graphene/silicon carbide composites, *Angew. Chem. Int. Ed. Engl.* 62 (2023) e202218664, <https://doi.org/10.1002/anie.202218664>.
- [42] H. Zhao, R. Yu, S. Ma, K. Xu, Y. Chen, K. Jiang, Y. Fang, C. Zhu, X. Liu, Y. Tang, L. Wu, Y. Wu, Q. Jiang, P. He, Z. Liu, L. Tan, The role of Cu₁-O₃ species in single-atom Cu/ZrO₂ catalyst for CO₂ hydrogenation, *Nat. Catal.* 5 (2022) 818–831, <https://doi.org/10.1038/s41929-022-00840-0>.
- [43] W.J. Li, L.F. Li, Q.N. Xia, S. Hong, L.J. Wang, Z.B. Yao, T.S. Wu, Y.L. Soo, H. Zhang, T.W.B. Lo, A.W. Robertson, Q.Y. Liu, L.D. Hao, Z.Y. Sun, Lowering C–C coupling barriers for efficient electrochemical CO₂ reduction to C₂H₄ by jointly engineering single Bi atoms and oxygen vacancies on CuO, *Appl. Catal., B* 318 (2022), <https://doi.org/10.1016/j.apcatb.2022.121823>.
- [44] C. Chen, X. Yan, Y. Wu, S. Liu, X. Zhang, X. Sun, Q. Zhu, H. Wu, B. Han, Boosting the productivity of electrochemical CO₂ reduction to multi-carbon products by enhancing CO₂ diffusion through a porous organic cage, *Angew. Chem. Int. Ed.* 61 (2022) e202202607, <https://doi.org/10.1002/anie.202202607>.
- [45] S. Tang, X. Zhou, S. Zhang, X. Li, T. Yang, W. Hu, J. Jiang, Y. Luo, Metal-free boron nitride nanoribbon catalysts for electrochemical CO₂ reduction: combining high activity and selectivity, *ACS Appl. Mater. Interfaces* 11 (2019) 906–915, <https://doi.org/10.1021/acsami.8b18505>.
- [46] Y. Zhang, T. Liu, X. Wang, Q. Dang, M. Zhang, S. Zhang, X. Li, S. Tang, J. Jiang, Dual-atom metal and nonmetal site catalyst on a single nickel atom supported on a hybridized BCN nanosheet for electrochemical CO₂ reduction to methane: Combining high activity and selectivity, *ACS Appl. Mater. Interfaces* 14 (2022) 9073–9083, <https://doi.org/10.1021/acsami.1c22761>.
- [47] J. Zhao, P. Zhang, T. Yuan, D. Cheng, S. Zhen, H. Gao, T. Wang, Z.-J. Zhao, J. Gong, Modulation of *CH₃O adsorption to facilitate electrocatalytic reduction of CO₂ to CH₄ over Cu-based catalysts, *J. Am. Chem. Soc.* 145 (2023) 6622–6627, <https://doi.org/10.1021/jacs.2c12006>.
- [48] J. Cho, S. Lee, S.P. Yoon, J. Han, S.W. Nam, K.-Y. Lee, H.C. Ham, Role of heteronuclear interactions in selective H₂ formation from HCOOH decomposition

- on bimetallic Pd/M (M = late transition FCC metal) catalysts, *ACS Catal.* 7 (2017) 2553–2562, <https://doi.org/10.1021/acscatal.6b02825>.
- [49] S. Tang, Q. Dang, T. Liu, S. Zhang, Z. Zhou, X. Li, X. Wang, E. Sharman, Y. Luo, J. Jiang, Realizing a not-strong-not-weak polarization electric field in single-atom catalysts sandwiched by boron nitride and graphene sheets for efficient nitrogen fixation, *J. Am. Chem. Soc.* 142 (2020) 19308–19315, <https://doi.org/10.1021/jacs.0c09527>.
- [50] Z.Z. Wu, X.L. Zhang, P.P. Yang, Z.Z. Niu, F.Y. Gao, Y.C. Zhang, L.P. Chi, S.P. Sun, J. W. DuanMu, P.G. Lu, Y.C. Li, M.R. Gao, Gerhardtite as a precursor to an efficient CO-to-acetate electroreduction catalyst, *J. Am. Chem. Soc.* 145 (2023) 24338–24348, <https://doi.org/10.1021/jacs.3c09255>.
- [51] P. Cheng, Y. Yang, N. Ahmad, S. Zhang, S. Huang, Ru₅₅ nanoparticles catalyze the dissociation of H₂O monomer and dimer to produce hydrogen: a comparative DFT study, *Int. J. Hydrog. Energy* 41 (2016) 3844–3853, <https://doi.org/10.1016/j.ijhydene.2016.01.017>.